Short Communication

A Comparative Investigation on corrosion Behaviors of High Pressure Die-cast Al-Si Alloys in 3.5% NaCl solution

Shangzhe Du[1,2], Chengcheng Zhang[3], Jie Zhu, Yulei Feng, Xin Pan, Jun Jia, Kai Feng[1,2,*], Zhuguo Li[1,2]

[1] Shanghai Key Laboratory of Materials Laser Processing and Modification, School of Materials Science and Engineering, Shanghai Jiao Tong University, Shanghai, 200240, China;
[2] Collaborative Innovation Center for Advanced Ship and Deep-Sea Exploration, Shanghai, 200240, China;
[3] Contemporary Amperex Technology Co., Ltd., Ningde, 352000, China
[*]E-mail: fengkai@sjtu.edu.cn

High pressure die-cast aluminum-silicon (Al-Si) alloys have been widely used to produce the power battery shell for new energy vehicles, and their corrosion resistance directly affects the durability of the battery. In this study, the corrosion behaviors of the high pressure die-cast AlSi10MgMn and AlSi9MnMoZr alloys were studied systematically for the first time by electrochemical, salt spray and immersion tests, and compared with the A356.2 and A380 alloys. The results indicated that all Al-Si alloys were composed of α-Al matrix and single-phase pure Si phase, while the presence of the $Al_{15}(FeMn)_3Si_2$ phase and $Al_{12}Mn_3Si_2$ phase was discovered in the AlSi10MgMn alloy and the AlSi9MnMoZr alloy, respectively. The potential of those phases was similar to that of the matrix, which made them better corrosion resistance. Potententiodynamic polarization studies revealed that the AlSi10MgMn and AlSi9MnMoZr alloys had obvious passivation regions compared with the A356.2 and A380 alloys. Salt spray and immersion test results showed that the AlSi9MnMoZr alloy had the lowest corrosion rate in the early period of the tests. Thus, the AlSi9MnMoZr alloy has the best corrosion resistance among the four alloys and is the ideal high pressure die-cast Al-Si alloy for power battery shells.

1. INTRODUCTION

The design and development of power battery shell materials have high requirements for their structural strength, light weight, durability, and corrosion resistance, which are essential for the safety

of power batteries. Consequently, high pressure die-cast aluminum-silicon (Al-Si) based alloys with their excellent properties are widely used in the power battery of new energy electric vehicles [1-3].

Silicon element, as one of the main alloying elements in high pressure die-cast Al-Si alloys, could contribute to reducing the shrinkage and density of the alloys [4]. However, the bulk polygonal primary Si phase will solidify in the alloy, when Si content is too high, which reduces the processing and mechanical properties of the alloys. Therefore, the silicon content of most cast alloys is limited to 5-17 wt.%. Besides, to obtain excellent mechanical and corrosion properties, high pressure die-cast Al-Si alloys are often optimized by adding other elements, such as Cu, Zn, Ti, Zr, Mn, Fe, Re, Ag, Sr, La, etc [5-12]. As a result, various brands of high pressure die-cast Al-Si alloys have been developed for the industrial field.

The A356.2 (ZL101A), A380 (AlSi8.5Cu3.5), AlSi10MgMn (Silafont-36), AlSi9MnMoZr (Castasil-37) alloys are four typically high pressure die-cast Al-Si based alloys, which all exhibit enough mechanical property for the power battery shell materials [7, 12-15]. However, the difference in their corrosion resistance will make the power battery shell materials different safety and service life. Therefore, it is necessary to conduct a comparative study on their corrosion resistance.

Although there are many researches about the A356.2 and A380 alloys fabricated by traditional casting, it is necessary to supplement the research on the corrosion resistance of the high pressure die-cast A356.2 and A380 alloys [16-18]. The AlSi10MgMn and AlSi9MnMoZr alloys are newly developed high pressure die-cast Al-Si alloys with high elongations [15]. The recent researches mainly focused on the control of their microstructure and mechanical properties, but their corrosion resistance remains to be studied. Therefore, in this study, the corrosion behaviors of the high pressure die-cast AlSi10MgMn and AlSi9MnMoZr alloys were studied systematically for the first time by electrochemical, salt spray, and immersion tests, and compared with the A356.2 and A380 alloys.

2. EXPERIMENTAL PROCEDURE

2.1. Alloy preparation and microstructural characterization

The alloys studied were the A356.2, A380, AlSi10MgMn, and AlSi9MnMoZr alloys, which were provided by CATL. The chemical composition of the studied alloys is listed in Table 1. The phases of the studied alloys were performed using a D8 Advance Da Vinci X-ray diffraction (XRD) instrument with Cu Ka radiation in the 2θ range of 20 °-110 °. Before the morphological observation, the surface of the studied alloys was successively abraded using different SiC abrasive papers, fine polished with 0.05 mm alumina (Al_2O_3), rinsed with ethanol, and air-dried. The microstructure and etched areas were observed by LEICA DM 4000 optical microscope (OM) and Nova NanoSEM 230 Compact field emission scanning electron microscope (SEM) attached to an energy dispersed spectroscopy (EDS). The chemical composition of the different phases of the studied alloys was quantified by EDS spot analysis, and the element distribution of the phases was identified by performing the Al, Si, Cu, Mg, and Mn EDS elemental mappings.

Table 1. Proposed chemical compositions of the A356.2, A380, AlSi10MgMn, and AlSi9MnMoZr alloys

Alloy	Composition/(wt.%)									
	Si	Cu	Mg	Fe	Ti	Mn	Zn	Sr	Others	Al
A356.2	6.5-7.5	≤0.1	0.30-0.45	≤0.12	≤0.2	≤0.05	≤0.05	-	-	bal.
A380	7.5-9.5	3.0-4.0	≤0.1	≤2.0	-	≤0.5	≤3.0		Sn≤0.35	bal.
AlSi10MgMn	8.5-10.5	<0.05	0.17-0.90	0.2-0.3	-	0.2-0.5	-	<0.001	Cr0.1-0.2	bal.
AlSi9MnMoZr	8.5-10.5	0.05	0.06	≤0.15	≤0.15	0.35-0.60	≤0.07	0.006-0.025	Zr≤0.3	bal.

2.2 Corrosion tests

For the electrochemical corrosion tests, the samples were 10 mm × 10 mm × 1.5 mm in size and wrapped with epoxy resin. The test surfaces of all samples were ground to 2000 grit using SiC abrasive papers, ultrasonically cleaned in acetone for 10 min, and air-dried before the experiments. Electrochemical tests were performed on a Zennium X electrochemical workstation with a three-electrode flat cell comprising the working electrode (the studied alloys), the reference electrode (Ag/AgCl), and the counter electrode (Pt). Potentiodynamic polarization tests were performed on electrodes polarized ±250 mV from the OCP at a scan rate of 1 mV/s after exposure to 3.5 wt.% NaCl solution for 1800s.

For the salt spray corrosion tests, the samples were 15 mm × 15 mm × 1.5 mm in size. The salt spray corrosion tests were conducted in 3.5 wt.% NaCl solution for 600 h at 35°C according to ASTM: B117 and the test sample was placed at an angle of 15~30 ° from the vertical plane of the test chamber. During the test, several samples were taken out every 24 h and placed for 48 h in the normal test atmosphere. After the corrosion products were removed by Cr_2O_3 + H_3PO_4 and HNO_3 solution, the weight loss induced by corrosion and corrosion rate was calculated and compared. Finally, SEM and EDS were used to observe the morphology of the corrosion layer.

For the immersion corrosion tests, the ratio of corrosive solution to the exposed area was above 0.2 mL/mm^2. The samples were 50 mm × 25 mm × 2 mm in size and were conducted in 3.5 wt.% NaCl solution for 10 d, 20 d, and 30 d at 35°C according to ASTM: G31-12a. After the corrosion products were removed by Cr_2O_3 + H_3PO_4 and HNO_3 solution, the weight loss induced by corrosion and corrosion rate was calculated and compared. The corrosion rate was calculated as the following equation：

$$\text{Corrosion rate} = (K \times W) / (A \times T \times D) \text{ mm/y} \qquad (1)$$

where $K = 8.76 \times 10^4$, W = Mass loss (mg), A-Area (cm^2), T-Time (h) and D - Density (2.7g/cm^3).

3. RESULTS AND DISCUSSION

3.1. Microstructure characterization

The XRD patterns of the Al-Si alloys are given in Fig. 1. The diffraction peaks of α-Al and pure Si phases indicated that all alloys included mainly α-Al and Si phases. In addition, the size and content

of other phases were small, so they were not detected by the XRD detector. They were found by SEM and EDS analysis, which would be discussed in detail below.
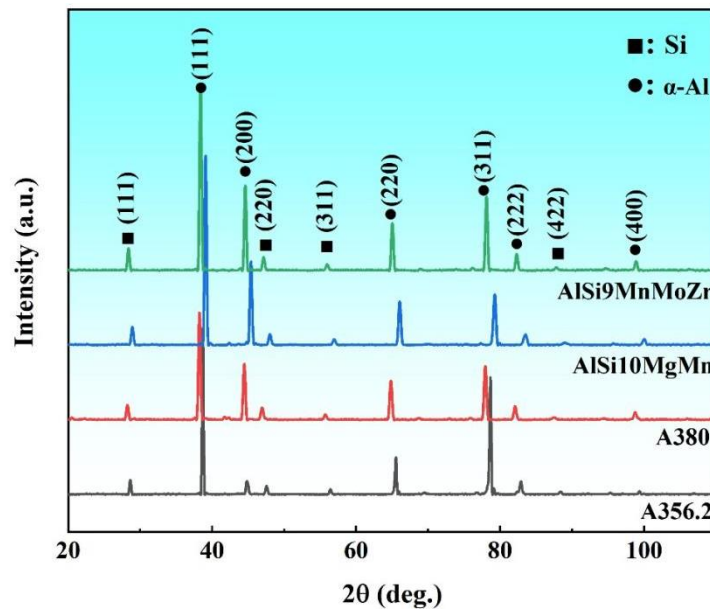

Figure 1. XRD patterns of the A356.2, A380, AlSi10MgMn, and AlSi9MnMoZr alloys

Microstructures and elemental distribution of the A356.2, A380, AlSi10MgMn, and AlSi9MnMoZr alloys are compared in Fig. 2. Lots of Si particles could be identified in the A356.2 alloy (Fig. 2a), while in the other alloys, Si existed in the form of the Al-Si eutectic structure. Due to the different content of Si in the alloys, the Si phase solidified in different forms in the alloys. According to Table 1, the Si content of the A356.2 alloy was relatively low, while in other alloys, the Si content reached or approached the eutectic point. Generally, Si has very low solubility in aluminum. Hence, it solidified as the pure Si phase in the A356.2 alloy. Part of the Cu element in the A380 alloy existed in the form of a solid solution in the Al-Si eutectic structure, and the other formed bone-like or needle-like Cu-rich phases (Fig. 2b). Besides, it can be seen that some Mn-rich phases distributed in the AlSi10MgMn and AlSi9MnMoZr alloys (Fig. 2c and 2d).

The chemical composition analysis of different positions of the A356.2, A380, AlSi10MgMn, and AlSi9MnMoZr alloys has been compared in Fig. 3 and Table 2. The dark areas of the four alloys were α-Al (Fig. 3 P1), which consisted of the majority of Al. Fig. 3 P2 was the Si particles in the A356.2 alloy. Fig. 3 P3, P5, and P7 were the Al-Si eutectic structure of the A380, AlSi10MgMn, and AlSi9MnMoZr alloys, respectively, containing a large amount of Al and Si. Fig. 3 P4 was the bone-like or needle-like Cu-rich phase, which has been confirmed to be Al_2Cu according to Table 2. The near-ellipsoidal phases in the AlSi10MgMn alloy were $Al_{15}(FeMn)_3Si_2$ according to the element analysis in Table 2 (Fig. 3 P6), which had also been confirmed in Borko's study [12]. Chemical composition of the $Al_{15}(FeMn)_3Si_2$ phase was: 61 % Al; 10, 3% Si; 13, 4% Fe; 2, 6% Cu; 13, 6% Mn, which was very close

to our study. The Mn-rich phases in the AlSi9MnMoZr alloy were $Al_{12}Mn_3Si_2$ (Fig. 3 P8) according to the element analysis in Table 2, which had also been confirmed in Franke's study [19].
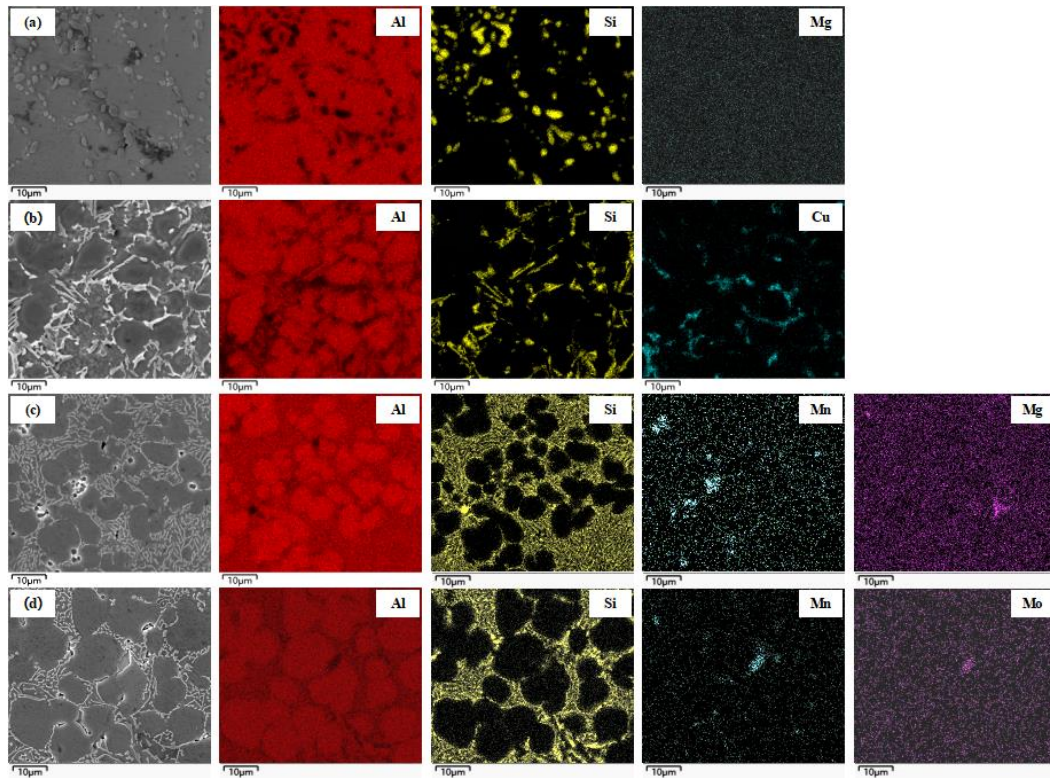

Figure 2. Microstructures of the (a) A356.2, (b) A380, (c) AlSi10MgMn, and (d) AlSi9MnMoZr alloys
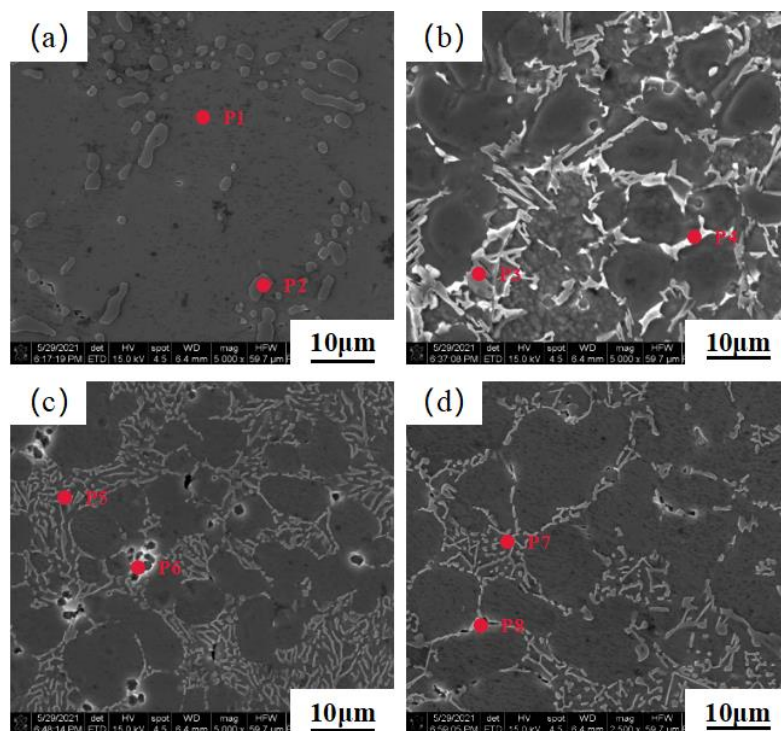

Figure 3. EDS spot chemical composition analysis of (a) A356.2, (b) A380, (c) AlSi10MgMn, and (d) AlSi9MnMoZr alloys

Int. J. Electrochem. Sci., 17 **(2022)** Article Number: 22125

6

Table 2. EDS spot chemical composition analysis of different positions in Fig. 3

Element/ (wt.%)	P1	P2	P3	P4	P5	P6	P7	P8
Al	99.4	28.3	63.3	55.0	73.8	70.1	60.0	71.1
Si	0.5	71.7	35.4	2.6	26.0	15.3	38.9	10.0
Cu	0.1	-	1.3	41.7	-	-	-	-
Mg	-	-	-	-	0.1	0.2	-	-
Mn	-	-	-	-	0.1	11.3	0.7	18.7
Fe	-	-	-	0.6	-	3.1	0.1	0.2

3.2 Corrosion behavior

3.2.1 Electrochemical corrosion studies

The corrosion behavior of the A356.2, A380, AlSi10MgMn, and AlSi9MnMoZr alloys was evaluated by potentiodynamic polarization tests in 3.5 wt.% NaCl solution. Fig. 4 shows variations of open circuit potential (OCP) values of the four alloys with time in 1800 s. The OCP values of all alloys became stable at 300 s, and the potential remained stable with minor fluctuations up to 1800 s. The change in OCP value was related to the formation of the surface layer, which could control the subsequent electrochemical reactions. The OCP values of the A356.2, A380, AlSi10MgMn, and AlSi9MnMoZr alloys were -0.474 V, -0.457 V, -0.603 V, and -1.009 V, respectively, indicating that different alloying elements of the four alloys altered the formation of the surface layer and the reactions on the surface.
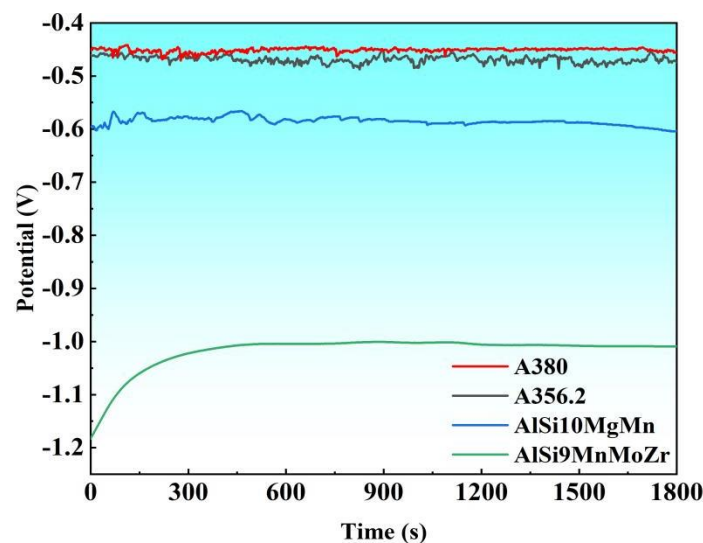

Figure 4. Variation of OCP values of the alloys in 3.5 wt.% NaCl solution with time in 1800 s

Fig.5 shows the potentiodynamic polarization curves of the alloys after the 1800 s of exposure. Table 3 lists the relevant potentiodynamic polarization parameters calculated based on the Tafel extrapolation method. Corrosion potential (E_{corr}) values of the A356.2, A380, AlSi10MgMn, and AlSi9MnMoZr alloys were −0.450 V, -0.415 V, -0.585 V, and -0.981 V, respectively. The result was in good agreement with the OCP values. According to the electrochemical corrosion behavior of the alloys, we could divide these four alloys into two categories: one has no obvious passivation, including the A356.2 alloy and the A380 alloy; the other has significant areas of passivation, including the AlSi10MgMn alloy and the AlSi9MnMoZr alloy. For the former category, when evaluating the corrosion resistance, the primary parameter was the corrosion current (I_{corr}) [20-22]. The alloys with the lower I_{corr} and the higher polarization resistance R_p showed better corrosion resistance. By Tafel fitting [23], we could find that the E_{corr} of the A356.2 and the A380 alloy was similar, but the I_{corr} of the A356.2 alloy was only a quarter of that of the A380 alloy and the R_p of the A356.2 alloy was more than ten times that of the A380 alloy, it was concluded that the corrosion resistance of the A356.2 alloy was better than the A380 alloy, which had been confirmed by the result of salt spray corrosion test and immersion corrosion test. For the latter category, the passivation zone of the alloys should be evaluated when estimating their corrosion resistance [24]. The corrosion current density increased slowly with the positive shift of the potential in the passivation zone, which meant the expansion of the corrosion behavior was greatly slowed down. The passivation region prevented the development of the corrosion behavior until the potential reached the breaking point (E_b). It was obvious that the AlSi9MnMoZr alloy had a more obvious passivation zone, and the breaking point (E_b) was -0.411 V, higher than that of the AlSi10MgMn alloy (-0.430 V). Although the I_{corr} of the AlSi10MgMn alloy was lower than that of the AlSi9MnMoZr alloy and the R_p of the AlSi10MgMn alloy was five times that of the AlSi9MnMoZr alloy, the latter presented better corrosion resistance with better passive film. Besides, the inspection of Table 3 revealed the values of the cathodic Tafel slopes (B_c) were higher than the anodic Tafel slopes (B_a) for the four alloys, indicating that the cathodic process controlled the electrochemical reaction.
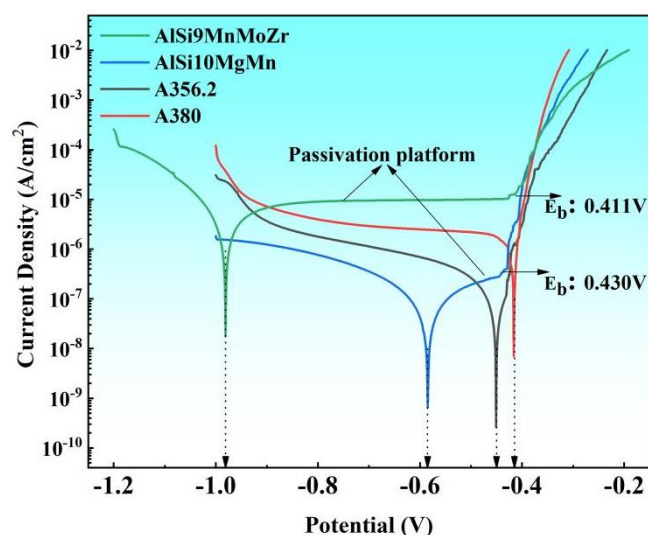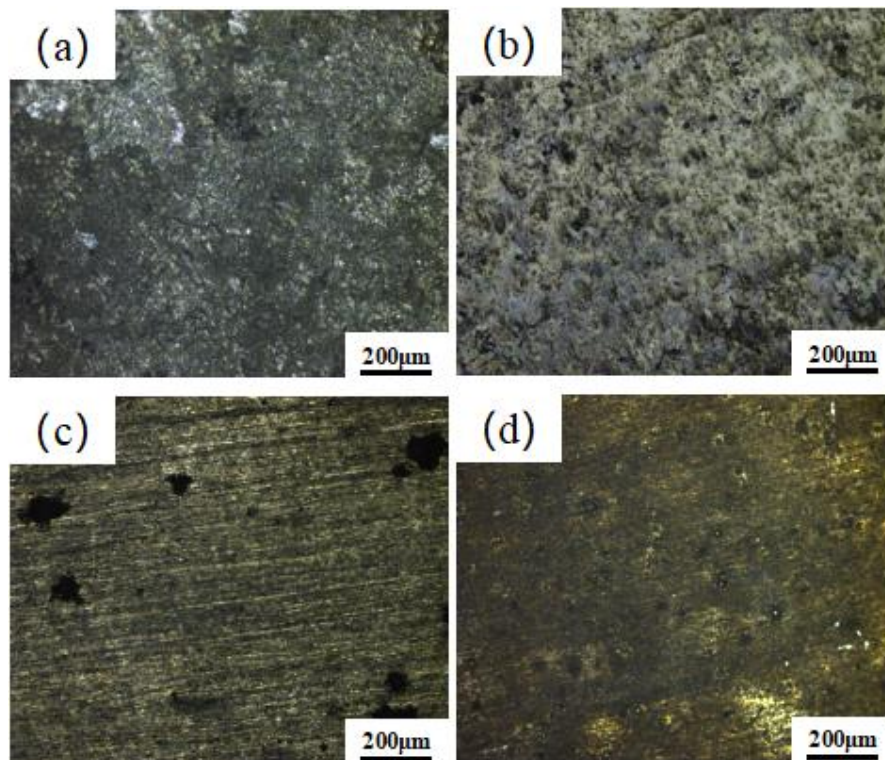

Figure 5. Potentiodynamic polarization curves of the alloys in 3.5 wt.% NaCl solution

Table 3. EDS spot chemical composition analysis of different positions in Fig. 3

Alloy	A356.2	A380	AlSi10MgMn	AlSi9MnMoZr
E_{corr} (V)	-0.450	0.415	-0.585	-0.981
I_{corr} (μA/cm^2)	0.446	1.79	0.74	2.12
R_p (kΩ·cm^2)	168	7.08	63	12.5
B_a (mV/dec)	127	24.6	171	98.8
B_c (mV/dec)	166	355	226	158

Fig. 6 shows the surface morphology after potentiodynamic polarization scanning of the alloys. The A356.2 and A380 alloys were mainly uniform corrosion after polarization according to their surface, and the corrosion products of the A380 alloy were more than those of the A356.2 alloy, which further confirmed its poor corrosion performance. For the AlSi10MgMn and AlSi9MnMoZr alloys, due to the existence of the passivation film, we could find lots of evidences of pitting corrosion. Besides, the pits of the AlSi10MgMn alloy were larger and deeper than those of the AlSi9MnMoZr alloy, indicating that the passivation film of the AlSi9MnMoZr alloy was more difficult to be destroyed, which was consistent with the result of the potentiodynamic polarization curves.

Figure 6. Surface morphology after potentiodynamic polarization scanning of the (a) A356.2, (b) A380, (c) AlSi10MgMn, and (d) AlSi9MnMoZr alloys

3.2.2 Salt spray corrosion studies

The corrosion weight loss and corresponding corrosion rates of the four alloys with different time of salt spray corrosion are shown in Fig. 7. Both corrosion weight loss and corrosion rate of the A380 alloy were much higher than those of the other three alloys, which further confirmed its poor corrosion resistance. At the initial stage of the test (0-13d), the corrosion rate of the A356.2 alloy was higher than those of the AlSi10MgMn and AlSi9MnMoZr alloys due to their passivation film. At the middle stage of the tests (14-22d), the corrosion rate of the AlSi10MgMn and AlSi9MnMoZr alloys increased gradually with the rupture of the passivation film and the intensification of local corrosion behavior. In the later stage of the tests (23-25d), the passivation film almost disappeared, and the galvanic corrosion caused by the second phase has been intensified, so the corrosion rate of the AlSi10MgMn and AlSi9MnMoZr alloys increased significantly.
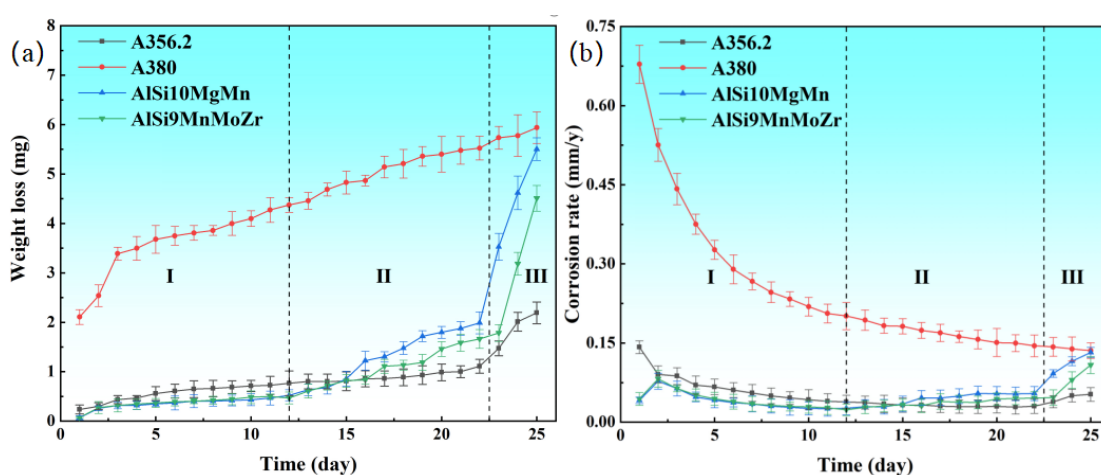

Figure 7. Changes in Weight loss (a) and corrosion rate (b) of the A356.2, A380, AlSi10MgMn, and AlSi9MnMoZr alloys at different days of salt spray corrosion tests, I, II, and III mean the early period of the tests, the middle period of the tests, and the later period of the tests, respectively

The microstructures of the four alloys in the early and late stages of salt spray corrosion tests are shown in Fig. 8. At the initial stage of the test (1d), the A356.2 and A380 alloys exhibited comprehensive and uniform corrosion morphology, while the A380 alloy has significantly severe corrosion and more corrosion products (Fig. 8a and Fig. 8b). The AlSi10MgMn and AlSi9MnMoZr alloys mainly exhibited pitting corrosion, while the AlSi10MgMn alloy had more obvious pitting, which was similar to the results of electrochemical corrosion (Fig. 8c and Fig. 8d). In the final stage of corrosion, all alloys exhibited comprehensive and uniform corrosion, and their surfaces were covered by corrosion products. The corrosion products on the surface of the A380 alloy were more and thicker, followed by the AlSi10MgMn alloy, while the A356.2 alloy is close to the AlSi9MnMoZr alloy (Fig. 8e, Fig. 8f, Fig. 8g, and Fig. 8h).

As mentioned above, there were a lot of Si particles in the A356.2 alloy. The Si particles were cathodic to the aluminum matrix by several hundred millivolts [13]. However, the effects of Si particles on the corrosion resistance were small because the silicon particles were highly polarized, resulting in

low corrosion current density. Therefore, the A356.2 alloy showed good corrosion resistance and a low corrosion rate even if it was not passivated. As for the A380 alloy, there was 3.0-4.0 wt.% Cu in the A380 alloy. A small amount of Cu solid dissolved in the matrix, while the rest precipitated near the Al-Si eutectic structure and formed Al_2Cu which has a positive potential and could increase the potential difference between the grain interior and grain boundary. These regions with a higher Cu content formed local microcells with a multi-electrode system around the aluminum matrix, which resulted in the continuous corrosion of the matrix [25]. As a result, the corrosion rate of the A380 alloy was the fastest among the four alloys. The AlSi10MgMn and AlSi9MnMoZr alloys were safeguarded by the passivation film at the initial stage of corrosion. Although there were $Al_{15}(FeMn)_3Si_2$ phases in the AlSi10MgMn alloy and $Al_{12}Mn_3Si_2$ phases in the AlSi9MnMoZr alloy, they had solution potentials almost the same as that of the aluminum matrix, the intergranular corrosion is slight and the initial corrosion rates of the AlSi10MgMn and AlSi9MnMoZr alloys are smaller than that of the A356.2 alloy. However, with the continuous destruction of the passivation film, the corrosion continued to intensify. The AlSi9MnMoZr alloy exhibited better corrosion resistance than the AlSi10MgMn alloy due to it having a more dense passivation film.
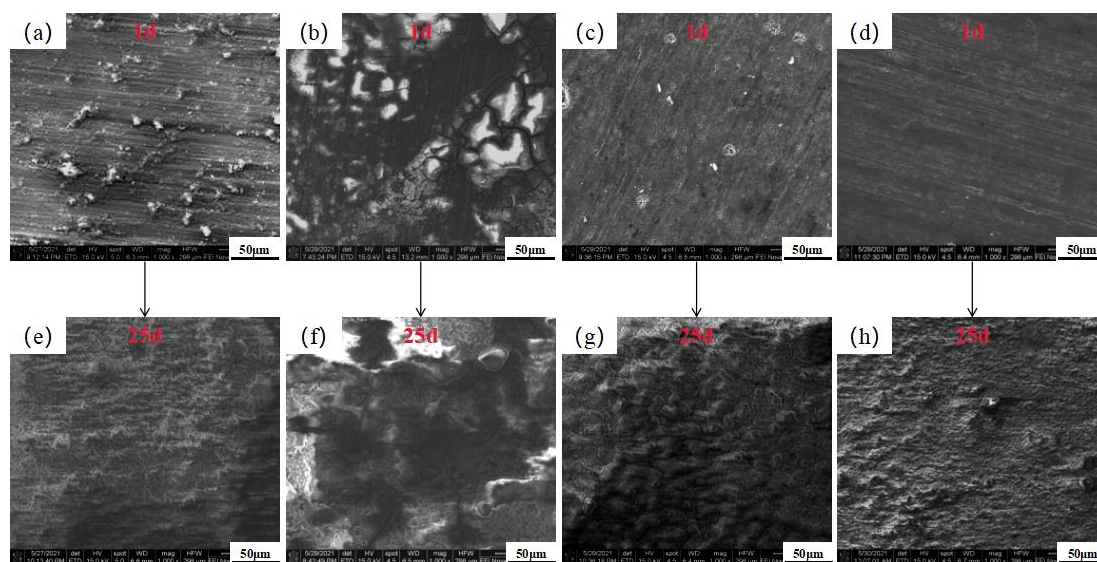

Figure 8. Surface morphology of different salt spray corrosion time of the (a) A356.2-1d, (b) A380-1d, (c) AlSi10MgMn-1d, (d) AlSi9MnMoZr-1d, (e) A356.2-25d, (g) A380-25d, (g) AlSi10MgMn-25d, and (h) AlSi9MnMoZr-25d alloys

3.2.3 Immersion corrosion studies

Immersion corrosion tests were conducted for 10 d, 20 d, and 30 d, and the corrosion rates were calculated based on the weight loss results. The corrosion rates of the A356.2, A380, AlSi10MgMn, and AlSi9MnMoZr alloys on different days of immersion corrosion tests are shown in Fig. 9. The corrosion rates of the four alloys all increased with the increase of immersion time, indicating that the corrosion accelerated with the increase of immersion time. With the continuous occurrence of corrosion, there

were increasingly defective positions on the surface of the alloys, and the corrosive Cl^- was more likely to be adsorbed on the defective positions, further triggering pitting corrosion, and constantly replacing OH^- on the surface of $Al(OH)_3$ to generate loose water-soluble $AlCl_3$, thus accelerating the corrosion. The corrosion rates were 0.058 mm/y for the A356.2 alloy, 0.149 mm/y for the A380 alloy, 0.064 mm/y for the AlSi10MgMn alloy and 0.048 mm/y for the AlSi9MnMoZr alloy after immersion in 3.5 wt.% NaCl solution for 10 d, indicating that the AlSi9MnMoZr alloy had the best corrosion resistance for early corrosion stages. The corrosion rates were 0.094 mm/y for the A356.2 alloy, 0.232 mm/y for the A380 alloy, 0.141 mm/y for the AlSi10MgMn alloy and 0.111 mm/y for the AlSi9MnMoZr alloy after immersion for 30d, indicating that the A356.2 alloy had better corrosion resistance for longer immersion corrosion tests. The deterioration of the corrosion resistance of the AlSi9MnMoZr alloy was due to the damage to the passivation film and the intensification of pitting corrosion behavior.
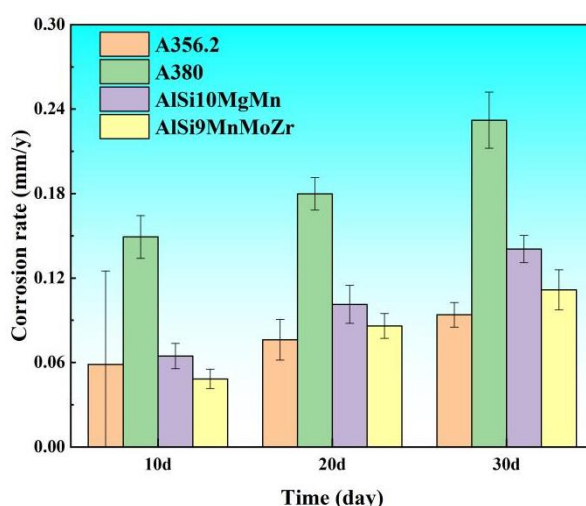

Figure 9. Corrosion rates of the A356.2, A380, AlSi10MgMn, and AlSi9MnMoZr alloys at different days of immersion corrosion tests

The macroscopic images of the samples as prepared and after different days of immersion with the corrosion products are listed in Fig. 10. It was obvious that the corrosion products covered the surfaces of all alloys after immersion in 3.5 wt.% NaCl solution. The surface of the corroded samples was darker, duller, and rougher than the as-prepared samples. Compared with the blank samples before immersion corrosion, the surfaces of the samples after immersion corrosion showed a black corrosion layer accompanied by gray dotted corrosion products [22, 26]. Interestingly, corrosion products were more identified for the A380 (Fig. 10b) and AlSi10MgMn (Fig. 10c) alloys, confirming their worse corrosion resistance compared to the A356.2 (Fig. 10a) and the AlSi9MnMoZr (Fig. 10d) alloys. The content of corrosion products on the surface of the A380 alloy was the most, indicating that the A380 alloy has the worst corrosion resistance. The A356.2 alloy showed better corrosion resistance when immersion for 20 d and 30 d, while the surfaces of the AlSi10MgMn and AlSi9MnMoZr alloys could find a lot of white corrosion products due to the damage to the passivation film and the intensification of pitting. The spot-like white corrosion products on the surface of the AlSi10MgMn alloy covered more

areas, indicating that the AlSi9MnMoZr alloy had better corrosion resistance, which was consistent with the salt spray corrosion results.
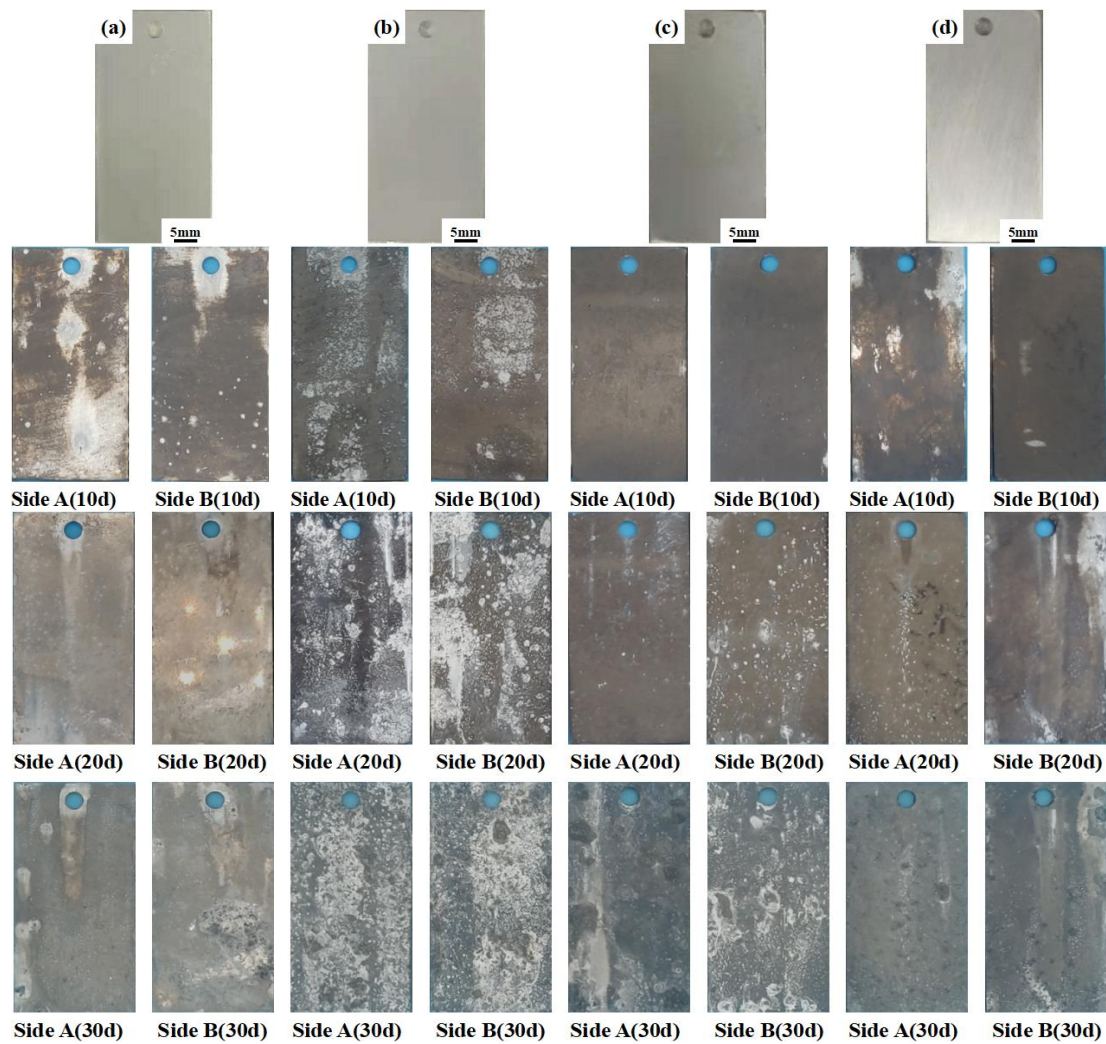

Figure 10. Macroscopic images of the (a) A356.2, (b) A380, (c) AlSi10MgMn, and (d) AlSi9MnMoZr alloys after immersion corrosion tests

The microstructure of the alloys after removing the corrosion products is compared in Fig. 11. The α-Al matrix of the four alloys was corroded. Due to the intergranular corrosion caused by the presence of Si particles in the A356.2 alloy, the matrix around the Si particles was corroded more seriously, and Si particles were even peeled off with the progress of corrosion. The local microcells in the A380 alloy made the matrix around the Cu-rich Al-Si eutectic structure and Al_2Cu phase corroded seriously, thus the microstructure of the A380 alloy showed the Al-Si eutectic structure blocked by lots of corrosion pits. The potential of the $Al_{15}(FeMn)_3Si_2$ phase in the AlSi10MgMn alloy and the $Al_{12}Mn_3Si_2$ phase in the AlSi9MnMoZr alloy was similar to that of the matrix, so the corrosion of the AlSi10MgMn and AlSi9MnMoZr alloys was relatively serious at the grain boundaries and the phase

boundaries of Al-Si eutectic structure after the destruction of the passivation film. The feature was more obvious in the AlSi10MgMn alloy because the AlSi9MnMoZr alloy has better corrosion resistance.
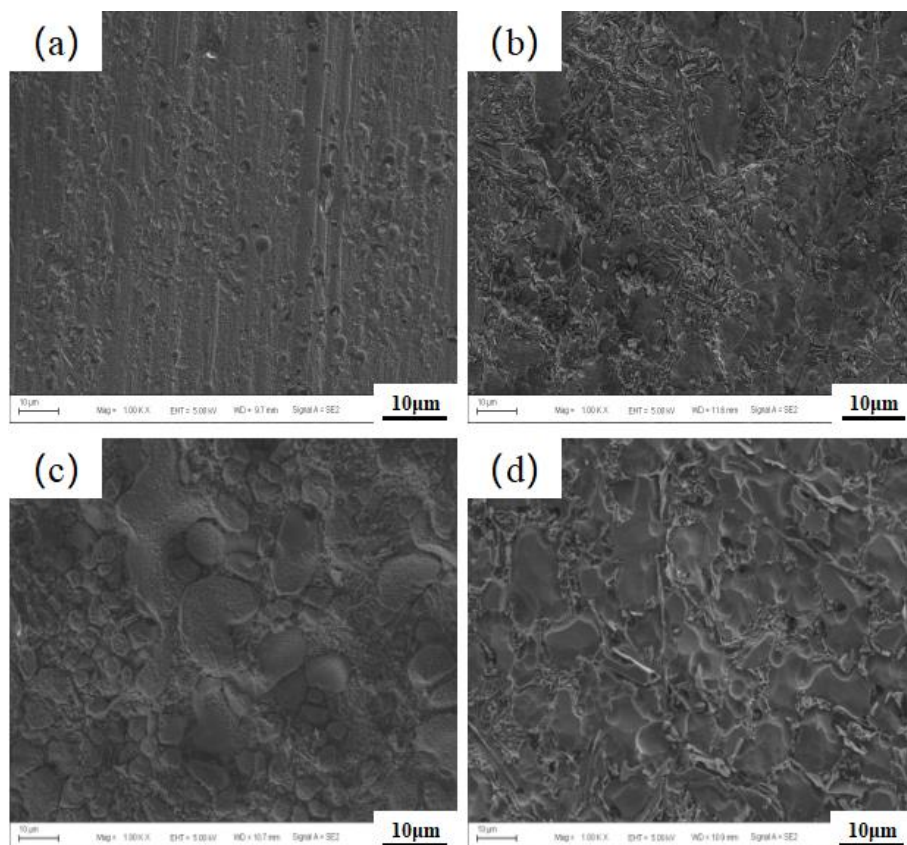

Figure 11. Microstructure of the (a) A356.2, (b) A380, (c) AlSi10MgMn and (d) AlSi9MnMoZr alloys after corrosion products removal
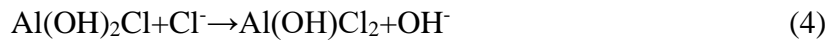
3.3 Corrosion products studies

The corrosion resistance of aluminum depends on the given environment and the stability of the passivation film. Without the passivation film of the A356.2 and A380 alloys, the uniformly corroded α-Al matrix could lead to lots of Al^{3+} generated at the initial stage of the corrosion reaction. Although the NaCl solution was neutral, the presence of Cl^- would seriously damage the passivation film[26]. With the damage to the passivation film and the continuous intensification of pitting, corrosion holes would form on the surface of the AlSi10MgMn and AlSi9MnMoZr alloys. The pitting continued to the depth of the matrix in the corrosion holes. With the accumulation of a large number of corrosion products, the occluded batteries further formed, and the Al^{3+} generated in the initial reaction would further undergo a hydrolysis reaction：

$$Al^{3+}+3H_2O \rightarrow Al(OH)_3+3H^+ \qquad\qquad (2)$$

Hydration of aluminum would generate a large number of H+, which made the solution inside the corrosion pit acidified so that the α-Al matrix around the corrosion pit was in the environment of an HCl solution which meant the matrix entered the state of activation [27]. Cl^- could pass through the

passivation film due to its small radius, so that a large number of Cl⁻ outside the corroded hole would continuously migrate to the pits and accumulate, increasing the Cl⁻ concentration in the corrosion pits. The H⁺ generated by hydration and Cl⁻ further promoted the dissolution of the matrix around the corrosion pits [28]. The reaction process is as follows:

$$Al(OH)_3+Cl^-\rightarrow Al(OH)_2Cl+OH^- \qquad (3)$$

$$Al(OH)_2Cl+Cl^-\rightarrow Al(OH)Cl_2+OH^- \qquad (4)$$

$$Al(OH)Cl_2+Cl^-\rightarrow AlCl_3+OH^- \qquad (5)$$

Therefore, the corrosion products on the outer surface were $Al(OH)_3$ and further decomposed into Al_2O_3 and some intermediate products containing Cl elements. Although the corrosion mechanisms of the four alloys were not the same, their corrosion products were similar. The microstructure of corrosion products is shown in Fig. 12. Corrosion products were amorphous particles whose particle size was mainly 40-120 μm (Fig. 12a and Fig. 12b), and the surface of the larger particles was also composed of some smaller and even nanoparticles (Fig. 12c). Besides, we found that the corrosion particles themselves were also composed of a large number of finer nanoparticles(Fig. 12d). Table 4 lists the EDS spot chemical composition analysis of corrosion products of different sizes in Fig. 12. The atomic ratio of Al and O at Fig. 12 P1 and P2 was close to 2:3, the atomic ratio of Al and O at Fig. 12 P3 was close to 1:3, and the atomic ratio of Al and O+Cl at Fig. 12 P4, P5, and P6 was close to 1:3. Therefore, the corrosion products are mainly mixtures of Al_2O_3 and $Al(OH)_3$ with some $Al(OH)_2Cl$ or $Al(OH)Cl_2$.
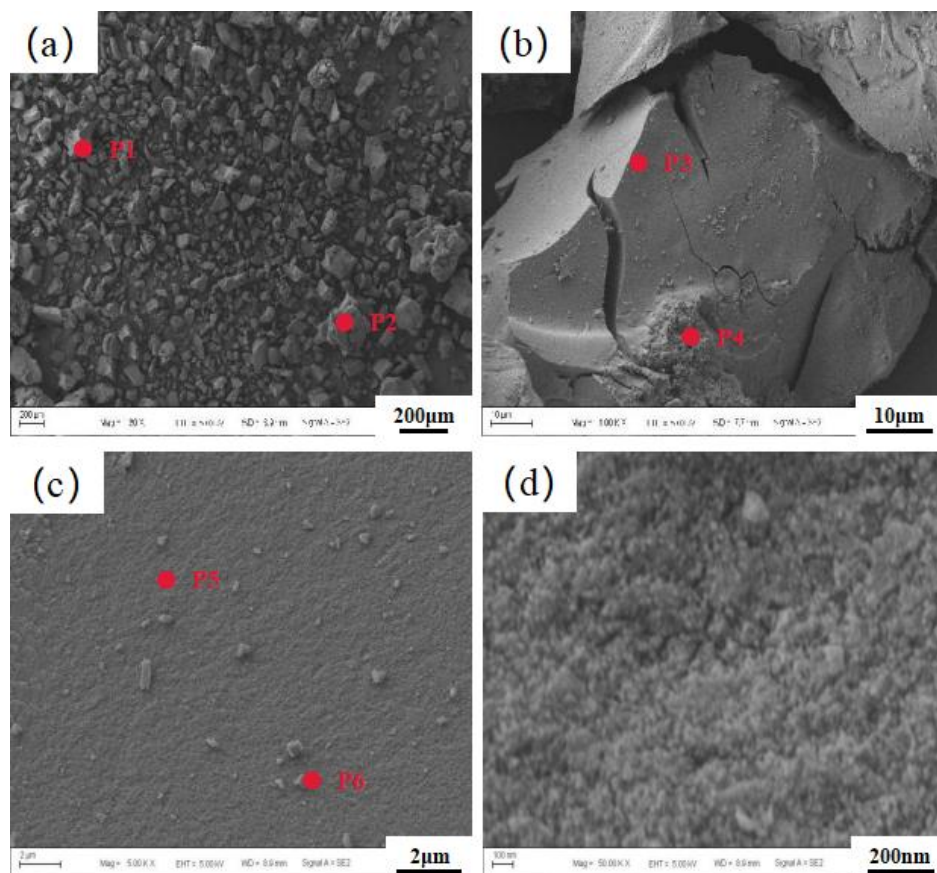

Figure 12. The microstructure of corrosion products

Table 4. Chemical composition analysis of corrosion products of different sizes in Fig. 12.

Element/ (at.%)	P1	P2	P3	P4	P5	P6
O	56.92	56.25	71.35	70.61	64.08	60.34
Al	43.08	43.75	28.65	25.86	27.32	26.74
Cl	-	0.77	-	3.54	8.60	12.91

4. CONCLUSIONS

Corrosion behavior of the A356.2, A380, AlSi10MgMn, and AlSi9MnMoZr high-pressure die-cast Al-Si alloys was studied, and the following conclusions were made:

1) Electrochemical corrosion studies revealed that the corrosion current (I_{corr}) of the A356.2 alloy was lower than that of the A380 alloy, and the surface topography was corroded uniformly after polarization. The AlSi10MgMn and AlSi9MnMoZr alloys had the passivation zone, and the surface topography showed many pits after polarization.

2) Salt spray corrosion studies showed that the corrosion rates of the AlSi10MgMn and AlSi9MnMoZr alloys were lower in the early stage of corrosion due to the protection of the passivation film. With the damage to the passivation film and the intensification of pitting corrosion, the corrosion rates of the AlSi10MgMn and AlSi9MnMoZr alloys accelerated in the late stage of corrosion tests, which were higher than that of the A356.2 alloy, but still smaller than that of the A380 alloy.

3) Immersion corrosion studies showed that the AlSi9MnMoZr alloy had better corrosion resistance with a short immersion corrosion time. With the increase of immersion corrosion time, the corrosion rates of the alloys all increased, but those of the A356.2, AlSi10MgMn, and AlSi9MnMoZr alloys were close.

4) Corrosion products studies showed that the corrosion products are mainly mixtures of Al_2O_3 and $Al(OH)_3$ with some $Al(OH)_2Cl$ or $Al(OH)Cl_2$.

5) It is understood from the results of the present investigation that the AlSi9MnMoZr alloy has the best corrosion resistance in 3.5 wt.% NaCl solution than the A356.2, A380, and AlSi10MgMn alloys.

References

1. J. Rams, and B. Torres, *Encyclopedia of Materials: Metals and Alloys*, Elsevier, (2021) Amsterdam, Netherlands.

2. M. Qi, Y. Kang, Q. Qiu, W. Tang, J. Li, and B. Li, *J. Alloys Compd.*, 749 (2018) 487.
3. F. Casarotto, A.J. Franke, and R. Franke, *Advanced Materials in Automotive Engineering*, Woodhead Publishing, (2012) Sawston, England.
4. M. Qi, Y. Xu, J. Li, Y. Kang, and Z. Wulabieke, *Corros. Sci.*, 180 (2021) 109180.
5. S. Wang, C. He, B. Luo, Z. Bai, and G. Jiang, *Vacuum*, 184 (2021) 109948.
6. S.K. Shaha, F. Czerwinski, W. Kasprzak, J. Friedman, and D.L. Chen, *Mater. Des.*, 83 (2015) 801.
7. C. Qiu, S. Miao, X. Li, X. Xia, J. Ding, Y. Wang, and W. Zhao, *Mater. Des.*, 114 (2017) 563.
8. T. Liu, M. Karkkainen, L. Nastac, V. Arvikar, I. Levin, and L.N. Brewer, *Intermetallics*, 126 (2020) 106814.
9. S.D. Kumar, M. Ravichandran, A. Jeevika, B. Stalin, C. Kailasanathan, and A. Karthick, *Ceram. Int.*, 47 (2021) 12951.
10. S.G. Shabestari, *Mater. Sci. Eng., A.*, 383 (2004) 289.
11. Y. Ma, Y. Liu, and M. Wang, *Mater. Chem. Phys.*, 276 (2022) 125321.
12. K. Borko, E. Tillová, and M. Chalupová, *Manuf. Technol.*, 16 (2016) 20.
13. H. Xie, Y. Cheng, S. Li, J. Cao, and L. Cao, *Trans. Nonferrous Met. Soc. China.*, 27 (2017) 336.
14. X. Qiu, N.H. Tariq, L. Qi, J. Wang, and T. Xiong, *Mater. Sci. Eng., A.*, 772 (2020) 138828.
15. X.Y. Jiao, Y.F. Zhang, J. Wang, H. Nishat, Y.X. Liu, W.N. Liu, H.X. Chen, and S.M. Xiong, *J. Mater. Process. Technol.*, 298 (2021) 117299.
16. C. Park, S. Kim, Y. Kwon, Y. Lee, and J. Lee, *Mater. Sci. Eng., A.*, 391 (2005) 86.
17. İ. Öztürk, G. Hapçı Ağaoğlu, E. Erzi, D. Dispinar, and G. Orhan, *J. Alloys Compd.*, 763 (2018) 384.
18. M. Karamouz, M. Azarbarmas, and M. Emamy, *Mater. Des*, 59 (2014) 377.
19. R. Franke, D. Dragulin, A. Zovi, and F. Casarotto, *Metall. Ital.*, 99 (2007) 19.
20. R. Arrabal, B. Mingo, A. Pardo, M. Mohedano, E. Matykina, and I. Rodríguez, *Corros. Sci.*, 73 (2013) 342.
21. S. Arthanari, J.C. Jang, and K.S. Shin, *J. Alloys Compd.*, 749 (2018) 146.
22. S. Arthanari, J.C. Jang, and K.S. Shin, *Trans. Nonferrous Met. Soc. China.*, 28 (2018) 2181.
23. J.R. Galvele, *Corros. Sci.*, 47 (2005) 3053.
24. Z. Hu, L. Wan, S. Lü, P. Zhu, and S. Wu, *Mater. Des.*, 55 (2014) 353.
25. F. Wen, J. Chen, and S. Han, *J. Mater. Res. Technol.*, 18 (2022) 3716.
26. S. Arthanari, J.C. Jang, and K.S. Shin, *J. Alloys Compd.*, 783 (2019) 494.
27. C. Haixiang and K. Dejun, *Mater. Chem. Phys.*, 251 (2020) 123200.
28. P. Fathi, M. Mohammadi, X. Duan, and A.M. Nasiri, *J. Mater. Process. Technol.*, 259 (2018) 1.